Analysis of TBM disc cutter performance based on the pressure distribution to optimize operational efficiency

International Journal of Rock Mechanics & Mining Sciences 204 (2026) 106590

Contents lists available at ScienceDirect

International Journal of Rock Mechanics and Mining Sciences

journal homepage: www.elsevier.com/locate/ijrmms

Research Paper

Analysis of TBM disc cutter performance based on the pressure distribution to optimize operational efficiency

Nestor Mejía *, Marilena Cardu, Pierpaolo Oreste

Department of Environment, Land and Infrastructure Engineering, Politecnico di Torino, Corso Duca degli Abruzzi, 24, 10129 Torino, Italy

ARTICLE INFO

Keywords:
TBM prediction models
CSM model
Excavation Specific Energy (SE)
Cutting force and normal force
Contact pressure distribution
Disc-rock interface

ABSTRACT

The excavation mechanism of Tunnel Boring Machine (TBM) cutter discs in rock tunnelling is highly complex. Because an extremely high contact pressure develops at the disc–rock interface, it triggers fractures in the rock and leads to chip formation. This study develops two predictive models that relate specific energy (SE) consumption in rock cutting to both the spacing-to-penetration (s/p) ratio and uniaxial compressive strength (UCS). The first model extends the Colorado School of Mines (CSM) framework by replacing its single contact-pressure distribution with alternative profiles, thereby revealing how the pressure profile governs the orientation and magnitude of disc-induced forces across different rock types. The second model is fully numerical. It uses contact-pressure profiles recorded in the laboratory with specialized testing machines (LCM and ILCM) for several rock types at reference penetrations, then generalizes these profiles across the full penetration range and computes the resulting cutting forces. The results are presented as characteristic curves that relate the SE to the s/p ratio and the UCS. The study shows that asymmetric and narrower profiles contribute to increased prediction uncertainty. The optimal s/p ratio is roughly 13–14 for low-strength rocks, drops to just under 10 for medium-strength rocks, and rises slightly above 10 for very high-strength rocks. A broader experimental pressure distribution profile better captures variations in contact pressure, enabling more stable and accurate predictions. Based on the performed analyses, knowledge of the contact pressure distribution is essential for identifying the optimal s/p ratio, which is associated with the minimum Excavation Specific Energy. This will thereby enable the proper design of the TBM cutter head and the effective management of the machine during tunnel advancement.

1. Introduction

A TBM is a large-scale equipment incorporating advanced engineering systems designed explicitly for tunnel excavation works.[1,2] The costs associated with installing, operating, and maintaining a TBM represent a considerable financial investment.[3] As a result, the construction industry strongly emphasizes maximizing operational efficiency through reduced energy and disc consumption while increasing excavation speed. Technically, optimal TBM performance minimizes component wear, lowers the risk of equipment failure, and decreases downtime occurrences, enhancing overall cost-effectiveness in tunnel construction projects.[4] In this context, numerous prediction models for TBM performance have been extensively documented in technical manuals, academic books, codes, journal articles, and engineering reports.[5–9] These models are adjusted using data obtained under specific geological and operational conditions. As a result, their predictive accuracy remains robust when applied to conditions under similar scenarios. However, their reliability diminishes when applied to geological formations that differ significantly from those originally considered.

Predictive models have been developed to enhance understanding of the interaction between rock and disc cutters, utilizing both empirical data and theoretical approaches. Empirical models[10–13] utilize historical data and employ regression, machine learning, case-based reasoning (CBR), statistical evaluation, and sensitivity analysis to establish correlations between machine operational parameters, rock mass characteristics, and performance indicators. These models enable the identification of optimal parameter ranges and their interactions to maximize operational efficiency. Conversely, numerical methods[14–17] like Finite Element Method (FEM), Discrete Element Method (DEM), Smooth Particle Hydrodynamics (SPH), and Computational Fluid Dynamics (CFD) incorporate constitutive models based on solid mechanics

* Corresponding author.
E-mail address: nestor.mejiaalmeida@polito.it (N. Mejía).

https://doi.org/10.1016/j.ijrmms.2026.106590
Received 10 July 2025; Received in revised form 25 May 2026; Accepted 26 May 2026

principles, rock mass characterization, tribological analysis to simulate rock and disc cutters interactions under realistic loading conditions, capturing the fracture mechanism.

Among the predictive models discussed, particular emphasis in the literature has been placed on those addressing load pressure distribution, given its direct impact on cutting efficiency. Rostami and Ozdemir[18] proposed a TBM prediction model based on force analysis to estimate cutting forces. A power function is employed to characterize the load pressure distribution, while an empirical correlation derived from extensive field data defines the maximum pressure. Cutting forces are expressed in differential form, relating load pressure distribution to the mechanical interaction between the cutter and the rock sample. Rostami[19] estimated load pressure distribution acting on a disc cutter during cutting by directly measuring stress at the lateral surfaces. Linear cutting tests were conducted on three different rock types at various penetration depths. The measurements were recorded using a disc cutter instrumented with strain gauges positioned 13 mm from the blade. Statistical analysis of the recorded strain gauge signals enabled the identification of the load distribution scenario that best matched experimental measurements. Findings revealed that the loading pressure deviates from theoretical distributions, exhibiting peak values concentrated at the centre of the contact zone, while the front and rear regions experience no pressure.

Using DEM simulation, Zhang et al.[20] conducted a parametric study to investigate contact pressure distributions and maximum contact pressures across four cutting scenarios. Load pressure profiles were characterized using Gaussian and Lorentzian distributions. The contact area was discretized into segments at an angular interval ($\Delta\beta$) of 1.0°. Furthermore, variations in the distribution parameters — controlling amplitude, position, and width — were evaluated regarding performance indicators and machine operational parameters. The findings indicated that maximum contact pressure depends solely on rock properties and does not depend on performance indicators or machine parameterss. Yang et al.[21] investigated the rock fragmentation mechanism by incorporating the cutting forces acting on the TBM disc cutter, the associated cutter wear, and the damage inflicted on the rock. The cutting forces were derived based on a parabolic load distribution to represent the normal contact stress at the cutter–rock interface. Cutter wear was evaluated using the frictional power principle, quantifying the mechanical energy expended to overcome sliding resistance. Furthermore, a second-order damage tensor characterized the evolution of rock damage. The results showed that cutter wear intensifies with increased penetration depth. Additionally, a larger installation radius amplifies the normal force, further intensifying cutter wear.

Numerical studies on rock cutting commonly refer to classical contact mechanics to approximate stress conditions at the cutter–rock interface. These studies typically employ implicit solvers[22] for static or quasi-static analyses, which are inherently limited in capturing fracture, large deformation, and material fragmentation. In contrast, explicit dynamic solvers implement some advanced algorithms, such as contact detection algorithms and element erosion methods.[23] These algorithms enable the simulation of the crack initiation, the chip formation, and the debris generation by identifying interacting surfaces during deformation and/or removing material once predefined failure thresholds are exceeded. Unlike classical analytical models and implicit schemes, explicit approaches physically represent the cutter–rock interaction, accounting for nonlinear fracture mechanisms and large-strain behaviour, without considering normal contact stress.[24]

Various TBM performance prediction models have been developed using different methodological approaches. Although these models provide valuable insights into cutter–rock interaction, alternative approaches are needed to better represent this interaction under varying geological and operational conditions. This study presents two complementary numerical models. The first model investigates whether alternative analytical pressure-load distribution functions can reproduce the experimentally observed SE–s/p correlation within the CSM framework, using two-dimensional correlation analyses between SE and the s/p ratio and three-dimensional response surface analyses involving SE, s, and p. Although the model reproduces trends comparable to the original CSM model, the analytical distributions fail to capture the experimentally observed nonlinear SE–s/p response. To address this limitation, the second model extends the force-analysis framework by incorporating experimentally derived discrete pressure-load distributions and machine-integrated sensor data from LCM experimental trials.[19] These distributions are used to estimate cutting forces and establish the SE–s/p relationship, which is then compared against experimentally observed correlations. By combining the generalization capability of the analytical framework with the physical representativeness of experimentally derived distributions, the second model reproduces the nonlinear SE–s/p response for rock types with UCS values below approximately 115 MPa.

2. Theory and technical context

2.1. Chip formation mechanisms in rock cutting

Replicating the rock breakage mechanism in the laboratory for direct observation and measurement could prove challenging. Such measurements require control points in the rock that cause cracks and disrupt the continuity of the medium intended for measurement. As a result, several theories have been proposed to explain the rock breakage mechanism, including concepts like tensile, fracturing, shearing, elasticity, and plasticity.[25] Alternative theories utilize indentation tests to measure the force and displacement of an indenter as it penetrates a rock specimen until the fracture occurs.[26,27]

Fig. 1(a)–(b) show a simplified disc cutter-rock interaction system and the fracture mechanism within the interlayed rock material. Thrusting the cutter into the rock induces localized stress,[28] creating a crushed zone.[29] Stress radiates from this zone's periphery, attenuating outward.[30,31] Continued loading initiates radial cracks, which propagate and intersect,[32] triggering shear failure and producing rock chips.[33]

2.2. Pressure distribution within the crushed zone

Defining the load distribution within the contact zone — the zone between the rock and the disc — is crucial for accurately predicting rock behaviour in the crushed zone. A well-characterized distribution function incorporating physically relevant parameters enhances its applicability in engineering contexts. Rostami and Ozdemir[18] proposed the CSM model — incorporated a power function (Eq. (1)) — to characterize the pressure distribution within the crushed zone. The distribution $P(\theta)$ is governed by the potential factors ψ and ϕ which is derived from p through a trigonometric relationship. For nonzero values of ψ, the contact pressure reaches its maximum value, P' (Eq. (2)) at the angle $\theta = 0$, and gradually decreases to zero as θ approaches the boundary angle ϕ. However, the distribution remains symmetric and invariant for ψ at zero. Fig. 2 shows the pressure distribution for various ψ values.

$$P_0 = P'\left(1 - \frac{\theta}{\phi}\right)^{\psi} \tag{1}$$

$$P' = C\sqrt[3]{\frac{s\,\sigma_c^2\,\sigma_t}{\phi\sqrt{R\,T}}} \tag{2}$$

where: C is a dimensionless coefficient characterizing the relationship between rolling force and vertical force; T is the cutter blade width, mm; σ_c defines the UCS of intact rock, MPa; σ_t represents the tensile strength of intact rock, MPa; and s is the spacing between cuts, mm.

The CSM is principally formulated based on Eqs. (3), (4). The model uses a single control point known as the resultant force angle (β). It specifies the position and angle of the resultant force (F_t) that acts on

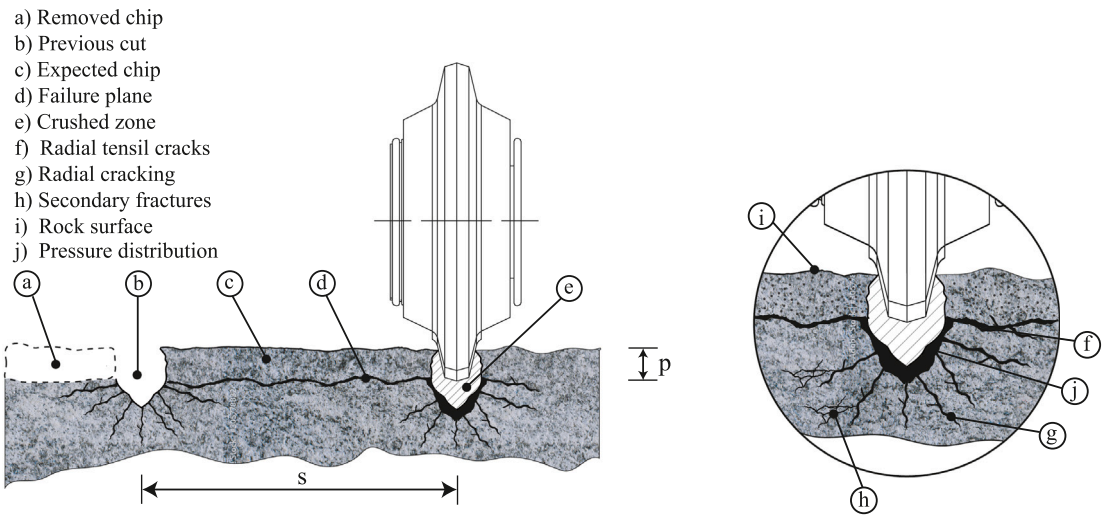

(a) Schematic illustration of fracture evolution in the rock. (b) Crack propagation.

Fig. 1. Fracture mechanism within the interlaying rock close to a disc cutter. p denotes the cutter's penetration depth, and s the spacing between cuts.

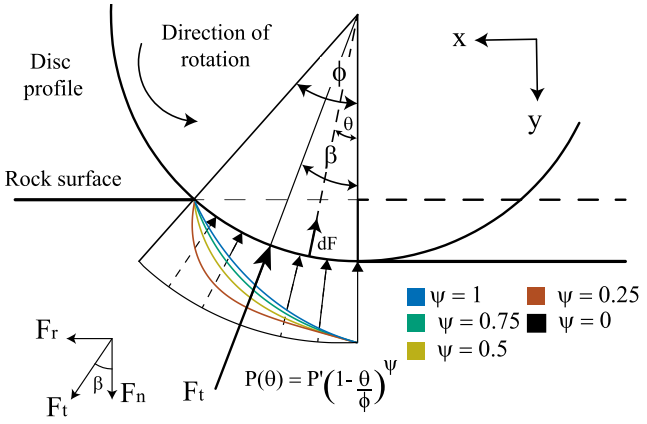

Fig. 2. General profile of the pressure distribution on the disc-rock contact surface, characterized by a power function. ψ denotes the potential factor, P' the maximum pressure value, F_t the resultant force, F_n the normal force, F_r the rolling force, and β the resultant force angle.

the disc relative to the normal force's direction. Eq. (5) expresses the normal force (F_n) and rolling force (F_r) components as the integral of an infinitesimal force element dF over an angle θ, capturing the cumulative force contributions over the range $0 \le \theta \le \phi$. Meanwhile, Eq. (6) represents the normal and rolling force components in terms of the resultant force and its orientation angle β and Eq. (7) defines the SE as the energy needed to excavate a unit volume of rock mass.[34]

$$dF = TRP' \left(1 - \frac{\theta}{\phi}\right)^{\psi} d\theta \tag{3}$$

$$F_t = \int_0^{\phi} TRP' \left(1 - \frac{\theta}{\phi}\right)^{\psi} d\theta \tag{4}$$

$$\begin{bmatrix} F_n \\ F_r \end{bmatrix} = \int_0^{\phi} dF \begin{bmatrix} \cos(\theta) \\ \sin(\theta) \end{bmatrix} d\theta \tag{5}$$

$$\begin{bmatrix} F_n \\ F_r \end{bmatrix} = F_t \begin{bmatrix} \cos(\beta) \\ \sin(\beta) \end{bmatrix} \tag{6}$$

$$SE = \frac{F_r}{s\ p} \tag{7}$$

A contribution of this study is presented in Eq. (8), which provides the general solution for the CSM model as formulated in Eq. (3), offering a more comprehensive framework for force analysis. The mathematical derivation is detailed in Appendix.

$$\begin{bmatrix} F_n \\ F_r \end{bmatrix} = TRP' \frac{\phi}{\psi + 1} \begin{bmatrix} \cos\left(\frac{\phi}{\psi+2}\right) \\ \sin\left(\frac{\phi}{\psi+2}\right) \end{bmatrix} \tag{8}$$

Alternatively, Yang et al.[21] evaluate the cutting forces by incorporating a parabolic function model (Eq. (9)). The boundary conditions are set such that $P(\theta) = 0$ at both $\theta = 0$ and $\theta = \phi$, with the maximum pressure $P(\theta) = P'$ at the symmetry axis, where $\theta = \phi/2$, as shown in Fig. 3. By applying these boundary conditions to Eq. (9), Eq. (10) is derived:

$$P(\theta) = a^2 R^2 \theta^2 + bR\theta \tag{9}$$

$$P(\theta) = 4P' \frac{\theta}{\phi}\left(1 - \frac{\theta}{\phi}\right) \tag{10}$$

where a and b are undetermined coefficients and R is the disc cutter's radius.

Zhang et al.[20] analyse the pressure distribution using the discrete element method, incorporating the Extreme (Eq. (11)), Gauss (Eq. (12)), and Lorentz (Eq. (13)) distributions, as shown in Fig. 3.

$$P(\theta) = P_0 + P'\ e^{\left(-e^{\frac{\theta-\theta_c}{\omega}} - \frac{\theta-\theta_c}{\omega} + 1\right)} \tag{11}$$

$$P(\theta) = P_0 + P'\ e^{-\frac{(\theta-\theta_c)^2}{2\omega^2}} \tag{12}$$

$$P(\theta) = P_0 + P'\ \frac{\omega^2}{(\theta - \theta_c)^2 + \omega^2} \tag{13}$$

where P_0 represents the initial pressure, θ_c is the contact angle corresponding to the maximum pressure P' (Eq. (2)), and ω is a parameter related to the width of distribution.

In contrast to these theoretical approaches, Rostami,[19] through direct measurement, observed that pressure distributions do not follow any explicitly defined mathematical function.[19]

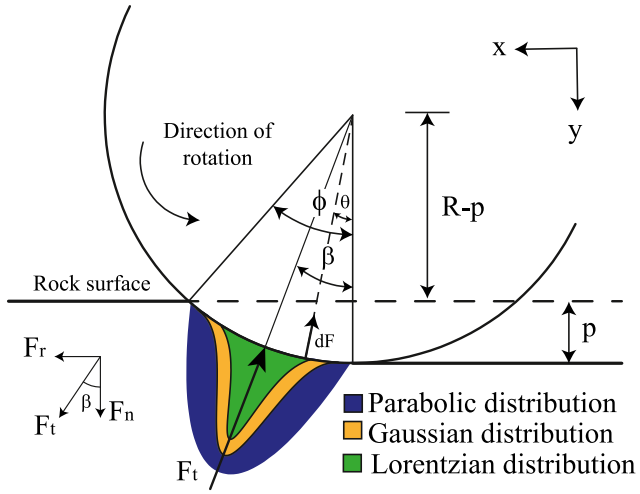

Fig. 3. The interaction zone between a disc cutter and the rock surface, with different types of pressure distributions. R denotes the radius of the disc cutter and p the cutter's penetration depth.

3. Performance of the CSM model considering alternative load distribution functions

Two numerical models were developed within the CSM framework, each replacing the original load distribution with an alternative analytical pressure profile, as shown in Fig. 4. Both models retained the CSM maximum contact pressure to preserve the standardized magnitude defined by the CSM, which accounts for rock mechanical properties including UCS and tensile strength. This allowed the effect of distribution shape to be isolated when evaluating predicted SE–s/p correlations. Several analytical distribution functions were examined to determine whether modifying the distribution form alone could reproduce the nonlinear behaviour observed experimentally.

Calibration and validation were performed using Xue's linear cutting tests on a TJ-TS500 machine.[35] Tests employed a constant-cross-section (CCS) disc cutter with a R of 216 mm and a T of 20 mm. C30 concrete specimens were tested across nine configurations: three cutter spacings (60, 80, 100 mm) and three penetration depths (4, 6, 8 mm). Cutting forces and SE were recorded in real time and correlated to s/p. The objective is to determine which analytical pressure distribution best reproduces the response observed in the experimental test.

The first model begins by assigning p as a vector and settings s as a constant. The methodology described in Section 2.2 is subsequently applied, replacing the original power-law function with the proposed analytical distributions. A numerical algorithm is then implemented to compute a solution that correlates SE with the s/p ratio.

The analysis considered the power distribution (Eq. (1)) for ψ values of 0, 0.5, and 1, as well as parabolic (Eq. (9)), Gaussian (Eq. (12)), and elliptical (Eq. (14)) distributions. Eq. (14) outlines the elliptical distribution, where a represents the semi-major axis and b is the semi-minor axis.

$$P(\theta) = P'\left(\frac{a\ b}{\sqrt{\left(b\ cos\left(\theta-\frac{\phi}{2}\right)\right)^2+\left(a\ sin\left(\theta-\frac{\phi}{2}\right)\right)^2}}-1\right) \tag{14}$$

The resulting curves show a monotonic increase (Fig. 5(a)) in the correlation between SE and s/p and a monotonic decrease (Fig. 5(b)) with p. Therefore, this model significantly deviates from the experimental results[35]; consequently, it does not adequately capture the influence of pressure distribution profiles on the variations in SE observed experimentally.

The second model treats s and p as vectors and incorporates an asymptotic limit in p: once the SE–p curve levels off, further increases in p produce negligible SE changes. At this point, a symmetry criterion is applied and the methodology used for the first model is employed. Fig. 6 presents 3D surface plots that illustrate model performance and reveal how variations in p and s influence SE across different pressure profiles. Additionally, Fig. 6 includes 2D contour plots that represent the pointwise differences between the SE outputs of the models, defined as $\Delta SE = SE_i - SE_j$, projected onto the s-p plane. SE_i corresponds to the row index and SE_j to the column index.

Fig. 6 reveals three insights. The first, and perhaps the most significant, the Parabolic and Gaussian models exhibit higher SE values with peaks in the 3D surface plots. They indicate localized pressure concentrations and more significant SE variations. The second insight concerns smoother SE distributions for the Power and Elliptical models. As a result, these cases are characterized by lower SE values and gradual transitions in the 3D surface plots. Such distributions are mathematically stable, but they may oversimplify the pressure distribution interactions and miss out on significant variations that interact in real-world rock-cutting scenarios. Lastly, the Gaussian distribution produces a large spectrum of the $\Delta SE = SE_i - SE_j$ in the contour plots, inferring higher SE variations than other distributions.

Fig. 7(a) shows the SE as a function of the s/p ratio. Green markers correspond to the LCM test data reported by Xue et al.[35], whereas blue markers show numerical predictions based on a Gaussian distribution. The numerical points are extracted on the plane $s = 57$mm—the section where SE attains its minimum. Fig. 7(b)–(c) shows the predictor model's response using input data.[35] The results are displayed as a 3D surface plot and a 2D contour graph, highlighting the correlation of SE according to different values of s and p. The blue contour projected onto the s–p plane indicates the model's low SE region. Specifically, the model identifies the lowest SE range, $19 \le SE \le 21\,\mathrm{MJ/m^3}$, within the ranges $2.5 \le p \le 8.0$ mm and $50 \le s \le 65$ mm, as shown in Fig. 7(c).

Although the model captures the influence of pressure distribution profiles on SE variations observed experimentally, an inconsistency between the experimental results and the model predictions remains. As illustrated in Fig. 7(a), experimental results indicate an optimal solution range for s/p between 14 and 16, whereas the numerical model shown in Fig. 7(a) predicts an optimal range from 4 to 8. This discrepancy suggests the current model is insufficiently robust to represent the experimentally observed rock–disc cutter interaction. Therefore, a new approach is proposed based on load pressure profiles and LCM performance data extracted from Rostami's experiments[19] for multiple rock types and penetration depths.

4. Numerical model development

The model was developed using directly measured pressure-load distributions from LCM experiments. In this approach, the maximum contact pressure is defined by the peak amplitude of the measured distributions, such that both the shape and magnitude inherently reflect the influence of rock mechanical properties and cutting conditions. The proposed model therefore operates independently of the original CSM maximum contact pressure formulation.

4.1. Data extraction and refinement

Rostami[19] reported load–pressure distributions obtained through direct measurements and statistical analysis, alongside LCM performance curves derived from integrated sensor data, including normal, rolling, and side forces and SE. Three rock types were tested: Indiana Limestone, Colorado Red Granite, and Umettela Basalt, with UCS of 50, 140, and 180 MPa, respectively. p of 2.5, 5.0, and 7.5 mm were applied for each rock type using a CCS disc cutter of 431 mm diameter and 11.5 mm blade width. Nine pressure gauges distributed along the cutter blade recorded the load–pressure response, enabling identification of

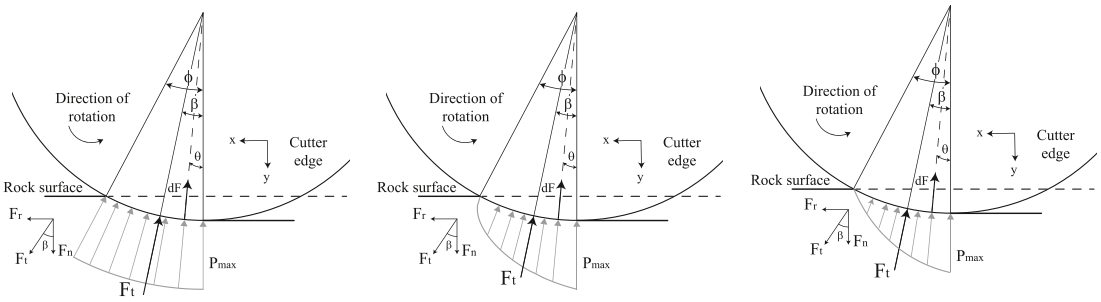

(a) Power distribution $\psi = 0$ (b) Power distribution $\psi = 0.5$ (c) Power distribution $\psi = 1$

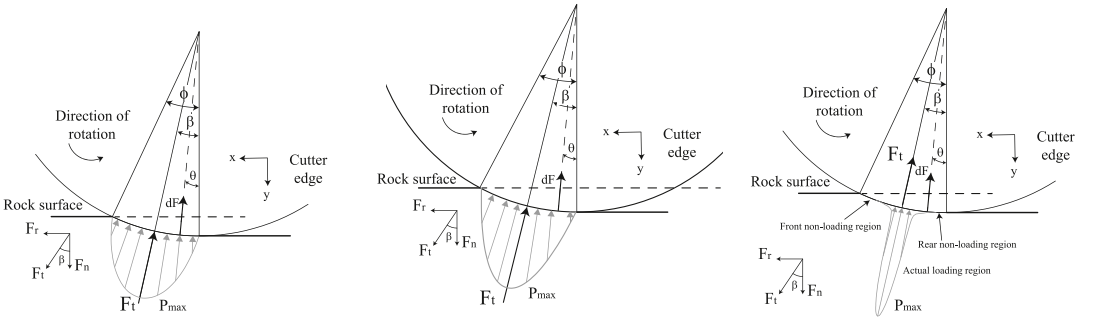

(d) Parabolic distribution (e) Elliptical profile (f) Gaussian profile

Fig. 4. Pressure distribution profiles at the disc–rock interface.

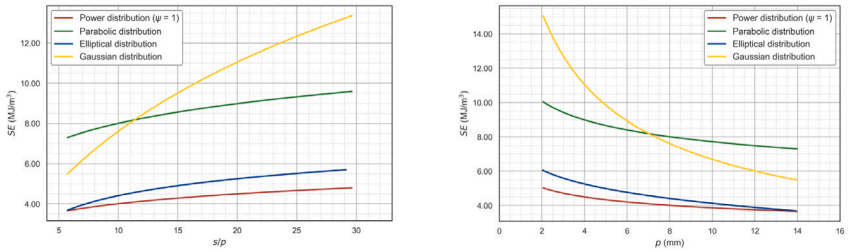

(a) Correlation between SE vs s/p. (b) Correlation between SE vs p.

Fig. 5. Numerical model response to different pressure distribution profiles for s = 8 cm.

loading and non-loading zones across all rock–depth combinations. The load–pressure distributions, LCM performance curves, and operational parameters reported by Rostami[19] constitute the experimental basis of the present study; the graphically presented data were digitized to produce structured datasets for numerical implementation.

The preprocessing stage employs an algorithm to isolate and individually process each data trend, minimizing noise and preserving data integrity. First, the images were converted to greyscale and processed by Gaussian smoothing to retain the essential information from the target trend. Subsequently, Otsu's algorithm[36] was applied for image binarization, with the option to invert the process depending on the contrast of the target curve.

Once the binary representation was obtained, a segmentation procedure was implemented using contour detection, followed by identification and merging steps to construct the distribution profiles in numerical form. After that, the merged contour points were converted into rectangular coordinates. This discrete set was then uniformly parameterized by computing the accumulated distance to define relative positions. New equally spaced points were generated along the total curve length, with coordinates determined through linear interpolation. Therefore, this numerical process extracts load distribution profiles reported by Rostami et al.[19] as discrete datasets, which are subsequently expanded to 8000 points (Fig. 8) based on a stochastic precision criterion essential for mathematical modelling and analysis. In this context, Fig. 9 shows the digitized load distribution data for each rock type and penetration depth derived from these experimental results.

4.2. Mathematical model

The discrete dataset comprises load distributions measured experimentally at penetration depths of 2.5, 5, and 7.5 mm, each recorded at 13 mm from the cutter-disc blade, hereafter referred to as the instrumented measurement arc.[19] The numerical code applies the Lagrange interpolation method to estimate intermediate load values at increments of 0.1 mm within the intervals from 2.5 to 5 mm and 5 to 7.5 mm. This approach constructs the polynomial interpolation as a

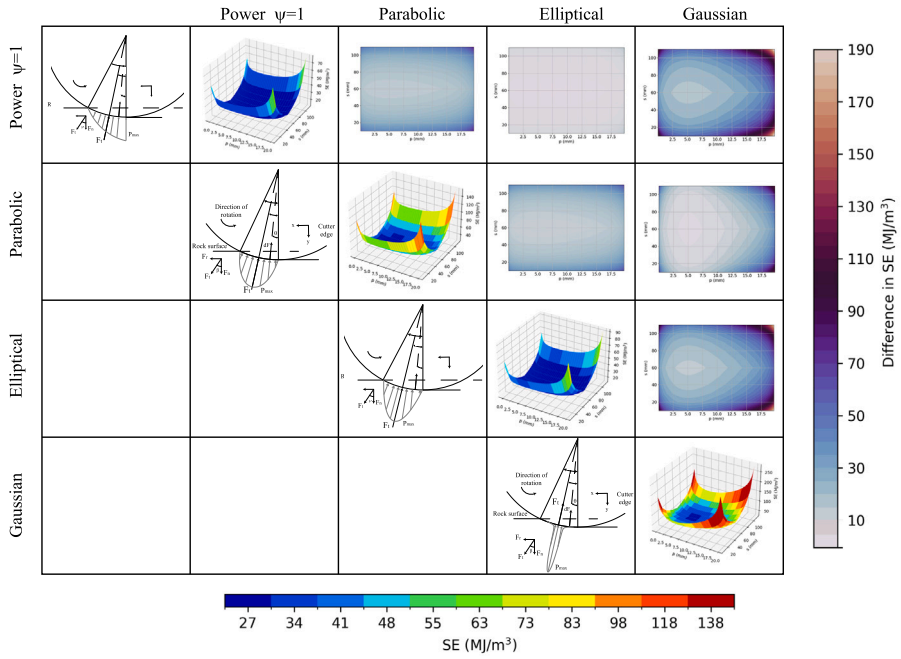

Fig. 6. 3D surface plots illustrate the variation in SE induced by different pressure distributions at the disc–rock interface. The analysis is based on the parameters reported by Xue et al.[35] (σ_c = 34.5 MPa, σ_t = 3.5 MPa, E = 9.98 GPa, ρ = 2.47 g/cm^3, R = 216 mm, T = 20 mm, s = 60, 80, 100 mm).

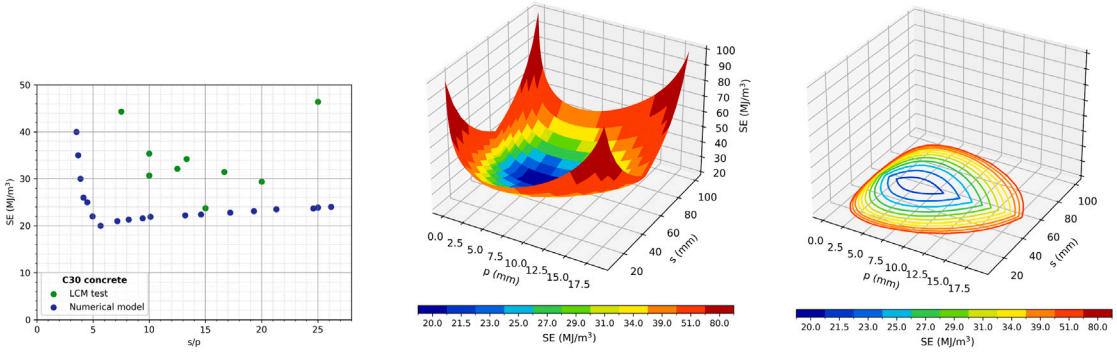

(a) s/p vs SE. (b) 3D surface. (c) 2D contour.

Fig. 7. Performance of the prediction model based on the Gaussian distribution, evaluated against experimental data for C30 concrete[35] (σ_c = 34.5 MPa, σ_t = 3.5 MPa, E = 9.98 GPa, ρ = 2.47 g/cm^3, R = 216 mm, T = 20 mm, s = 60, 80, 100 mm).

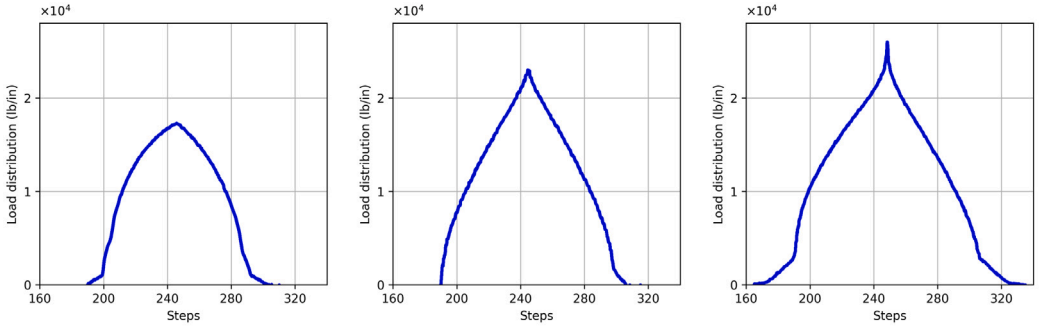

(a) p = 2.5 mm. (b) p = 5 mm. (c) p = 7.5 mm.

Fig. 8. Discrete dataset for Indiana Limestone based on the results reported by Rostami.[19]

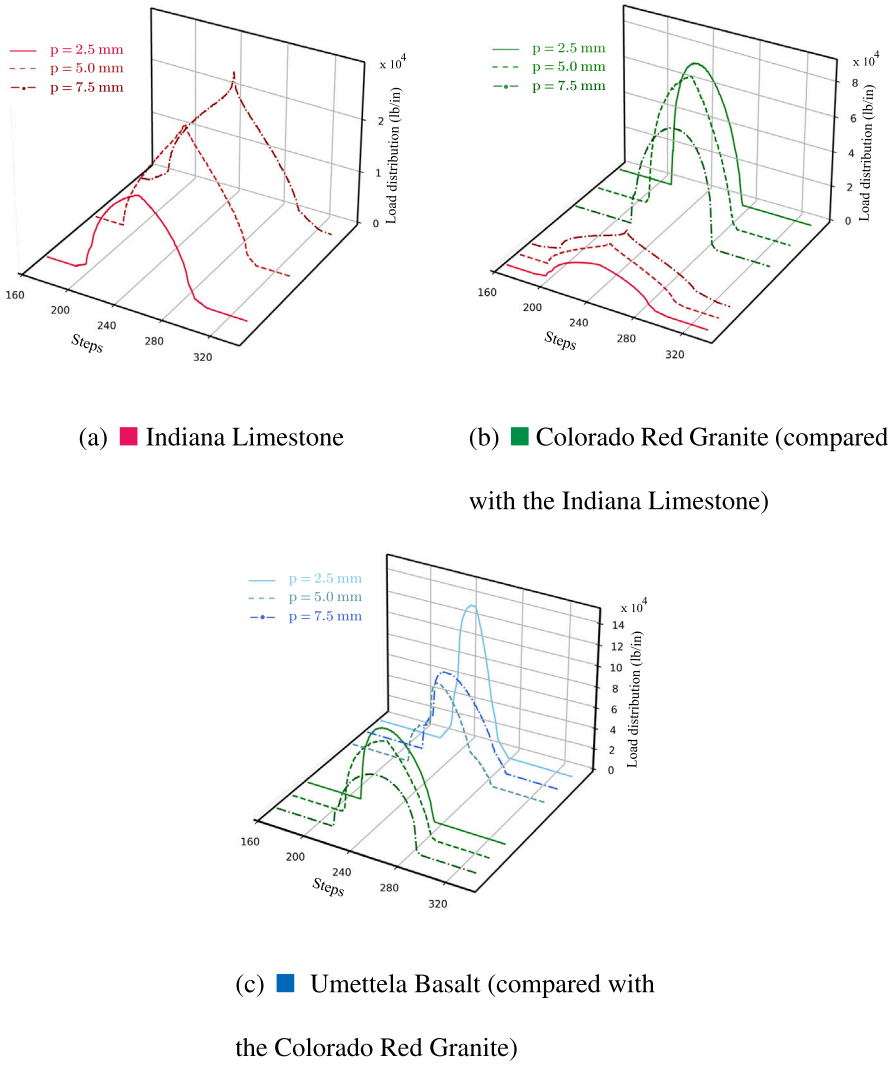

(a) ■ Indiana Limestone

(b) ■ Colorado Red Granite (compared with the Indiana Limestone)

(c) ■ Umettela Basalt (compared with the Colorado Red Granite)

Fig. 9. Digitized load distribution values for three rock types, based on the results reported by Rostami.[19]

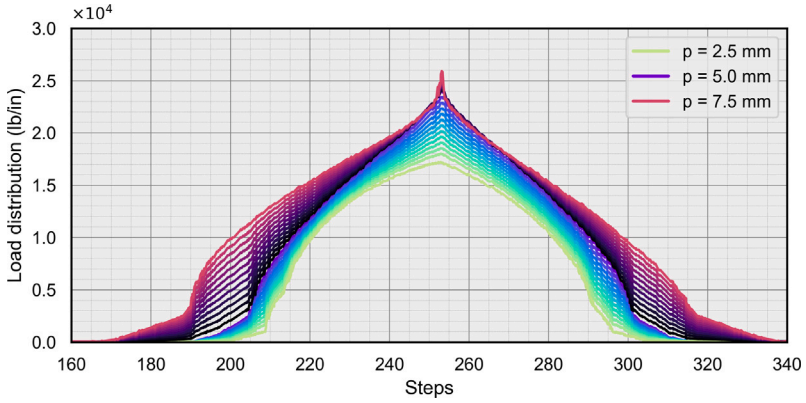

Fig. 10. Load distribution mapping for Indiana Limestone at varying penetration depths.

weighted sum of Lagrange basis polynomials, each distinctly associated with a specific reference depth. Consequently, interpolated load values were computed across the defined intervals, and the resulting load distributions, were presented using the same units as in the original study,[19] as shown in Fig. 10.

The Monte Carlo integration was employed to approximate the area under a discrete load distribution. The zone information[19] is employed to delineate the loading and corresponding front and rear non-loading regions along the measurement arc at the experimental penetration depths (Fig. 4(f)). Linear interpolation is then applied to define these loading and non-loading regions within the numerical interval of discrete measurement arc values and the penetration depth series. β is subsequently computed from these discrete load distributions using numerical integration.

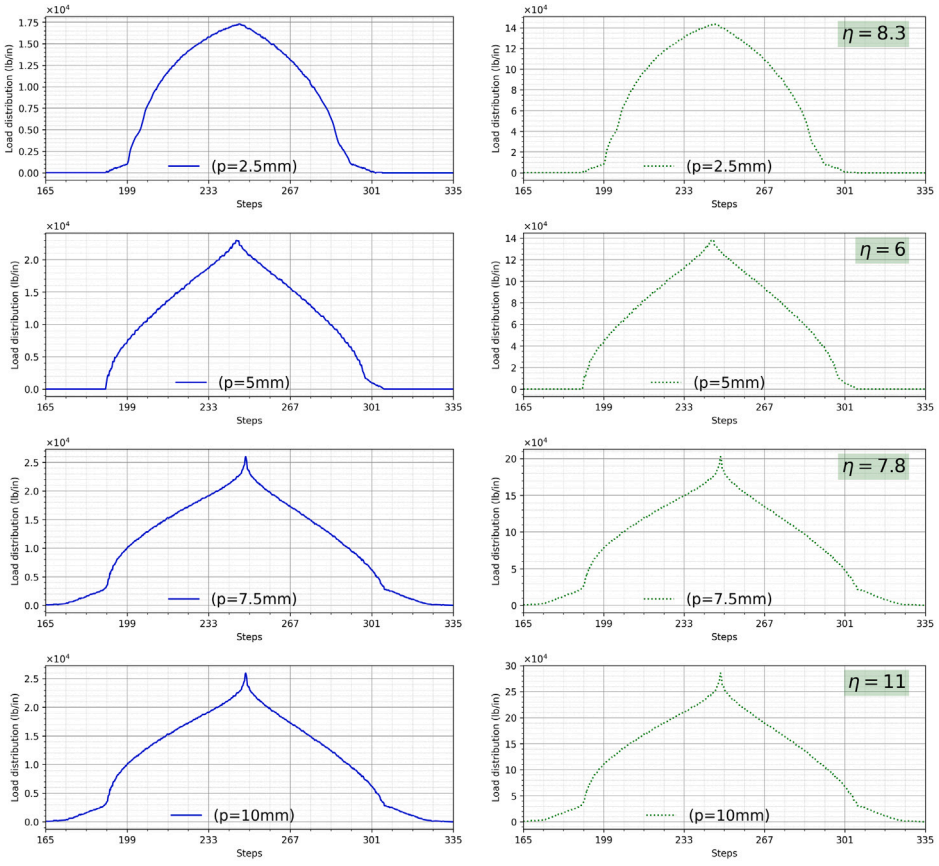

(a) Experimental distribution. (b) Amplified distribution.

Fig. 11. Amplified load distributions for Indiana Limestone at $p = 2.5$ mm, 5.0 mm, 7.5 mm, and 10 mm.

The Fourier transform was applied to the experimental load distribution to identify its frequency components. Subsequently, an amplified load distribution was created by scaling the experimental data while preserving its shape characteristics (Fig. 11(a)). This procedure enabled the extrapolation of the load distribution from the instrumented measurement arc to the contact arc, which defines the zone of cutter disc blade-rock interaction. The amplification factor (η) was calibrated so that the SE - s/p curves derived from the numerical model aligned with the characteristic curve obtained from internal data (machine-integrated sensors), as reported in the experimental study.[19] The calibration procedure used an iterative loop to generate multiple amplified load distributions and their corresponding numerical SE - s/p responses. The ten best candidate responses were selected from these iterations, and the final amplification factor was chosen based on the overall agreement between the numerical curves and the reference response from the machine-integrated sensor data. The resulting amplified distributions (Fig. 11(b)) retained the fundamental frequency content of the original data and extended their magnitudes to match the characteristic curves described in Section 4.1. Finally, the numerical model utilized this amplified discrete load distribution and repeated the previously described numerical sequence to obtain the numerical SE - s/p curves.

4.3. Assumptions

The characteristic experimental SE–s/p curves, particularly for Colorado Red Granite and Umettela Basalt, deviate from the theoretically predicted convex trend.[37] Typically, the SE decreases initially as the s/p ratio increases, attains a clear optimal minimum and subsequently increase again. Thus, data processing must align these experimental curves with theoretical expectations. Consequently, an additional data point is introduced based on two specific assumptions to extend the SE–s/p experimental characteristic curves[19] beyond the observed ranges, alongside a further assumption for numerical modelling purposes.

The first assumption specifies the angle β as 50% of angle ϕ, justified by experimental observations indicating that angle β varies within approximately ±10%. The second assumption relies on the experimentally observed F_n–p correlation presented in the characteristic curves, which exhibits near-linearity, supporting the assumption of a constant slope. Employing the trigonometric relationship between $tan(\beta)$ and F_n enables the determination of the F_r. Extended SE values can be computed using Eq. (7), allowing extrapolation beyond the experimentally measured SE–s/p range. For this purpose, the numerical model introduces a single extra data point, defined at 10, 12.5, or 15 mm penetration depth depending on the rock type, which adopts a load distribution profile similar to that of the nearest existing point. However, it employs a different factor derived from the previously stated assumptions based on the SE–s/p data from the characteristic curves.

Furthermore, a solver is implemented to interpolate and generate a new load distribution for a given UCS within the tested range. Once this load distribution is determined, the numerical code iterates through the computational sequence described in Section 4.2 to derive the numerical SE–s/p curves.

5. Results and observations

Solutions derived through the numerical model exhibit variability in minimum and maximum values across multiple iterations due to

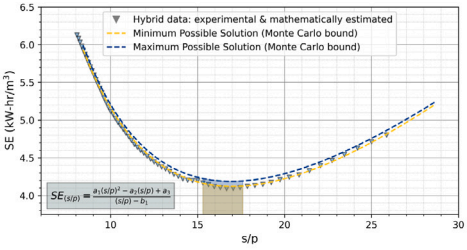

(a) Indiana Limestone

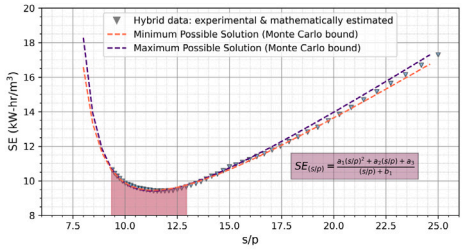

(b) Colorado Red Granite

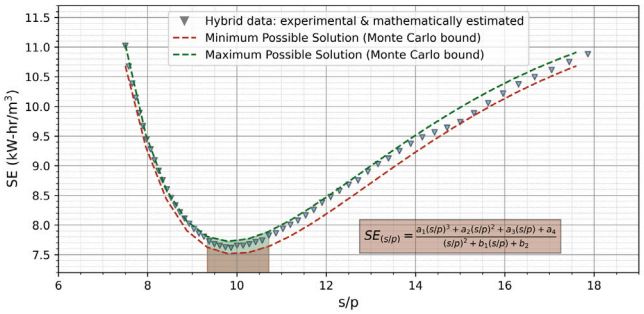

(c) Umettela Basalt

Fig. 12. SE–s/p correlation derived from the numerical model, based on experimental results from Rostami.[19]

the inherent randomness of the sampling process, as shown in Figs. 12(a)–(c). The Indiana Limestone model shows minimal uncertainty in the range $8 \leq s/p \leq 28$. Within this interval, Fig. 12(a) shows narrow Monte Carlo bounds and tightly grouped SE points near the minimum, confirming that the model's predictions are stable and consistent.

Fig. 12(b) shows that Monte Carlo bounds exhibit a tight alignment around the SE minimum at $s/p \approx 10$–11, indicating high precision, in the SE range of 7.5–10.3 kW h m^{-3}. However, Fig. 12(b) also reveals the onset of bound divergence, accompanied by a marked increase in the dispersion of the SE, as s/p increases. Therefore, the model's accuracy declines outside this interval. The Umettela Basalt model (Fig. 12(c)) shows narrow Monte Carlo bounds around the SE minimum at $s/p \approx 9$–16, indicating strong model performance in this range. Once s/p exceeds 16, the widening gap between the bounds indicates rising uncertainty.

Curve-fitting analyses reveal distinct behaviours among different rock types. Indiana Limestone and Umettela Basalt conform to a rational function characterized by a second-degree numerator and a first-degree denominator, effectively describing their smooth, concave SE–s/p relationships. Conversely, Colorado Red Granite needs another type of rational function, employing a third-degree numerator and a second-degree denominator, which are more sensitive to variations in input parameters. Therefore, a singular curve formulation may not adequately describe the behaviour of all rock types.

Fig. 13 presents a generalized SE–s/p relationship across varying UCS ranges, using the model performances of Indiana Limestone, Colorado Red Granite, and Umettela Basalt as reference points for interpolation. As expected, the model response increasingly adopts the functional form of the original dataset as the UCS approaches its reference value. An increase in UCS corresponds to higher SE values and a shift of the optimal s/p ratio towards lower values aligning with realistic rock-cutting conditions.

A clear correlation exists between UCS and the slope of the SE with respect to the s/p ratio, as shown in Fig. 13. Experimental data[17,35] and the proposed model all show that rocks with higher UCS exhibit steeper SE gradients near the optimum s/p, revealing greater sensitivity to deviations from optimal cutting conditions. This behaviour is pronounced in high-strength materials—Hwangdeung granite (183 MPa), Palgwang gneiss (124 MPa), and granite (203.5 MPa)[17]—whose SE rises sharply once s/p moves away from the optimum, matching model predictions for UCS ≥ 120–180 MPa. Conversely, lower-strength rocks such as Yeongweol limestone (64 MPa) and Hudong granite (91 MPa)[17] have flatter slopes, consistent with model curves for UCS ≈ 60–90 MPa. The model's ability to capture these UCS-dependent sensitivities confirms its robustness for predicting energy consumption in linear cutting mechanics across a broad spectrum of rock strengths.

Statistical error analysis for rock types with UCS values below 115 MPa is reported in Table 2. After excluding outliers identified by a relative error criterion exceeding 30%, SE predictions yielded MAE, RMSE, and MAPE values of 0.4950, 0.5656, and 9.13%, respectively, with $R^2 = 0.9091$, indicating close agreement between predicted and experimental values. For the s/p ratio, MAE, RMSE, and MAPE values of 1.492, 2.01, and 12.28% were obtained, with $R^2 = 0.62$, reflecting moderate predictive capability and greater unexplained variability relative to SE. Predictive reliability is therefore higher for rock types with UCS values below approximately 115 MPa. For higher UCS values, relative errors increase substantially — in several cases exceeding 100% — significantly reducing predictive reliability.

Table 1 presents a comparative analysis between the proposed numerical framework and previous LCM experimental results across different rock types. The framework reproduces SE–s/p behaviour with close agreement for low- to medium-strength rock classes, including limestone, granite, and Carrara marble. The statistical performance evaluation summarized in Table 2 indicates good predictive capability for SE and moderate predictive capability for the s/p ratio within the validated UCS interval. The results indicate a progressive increase in relative error with increasing UCS, leading to the identification of an approximate applicability threshold at 115 MPa, beyond which predictive reliability decreases significantly. Several rock classes within

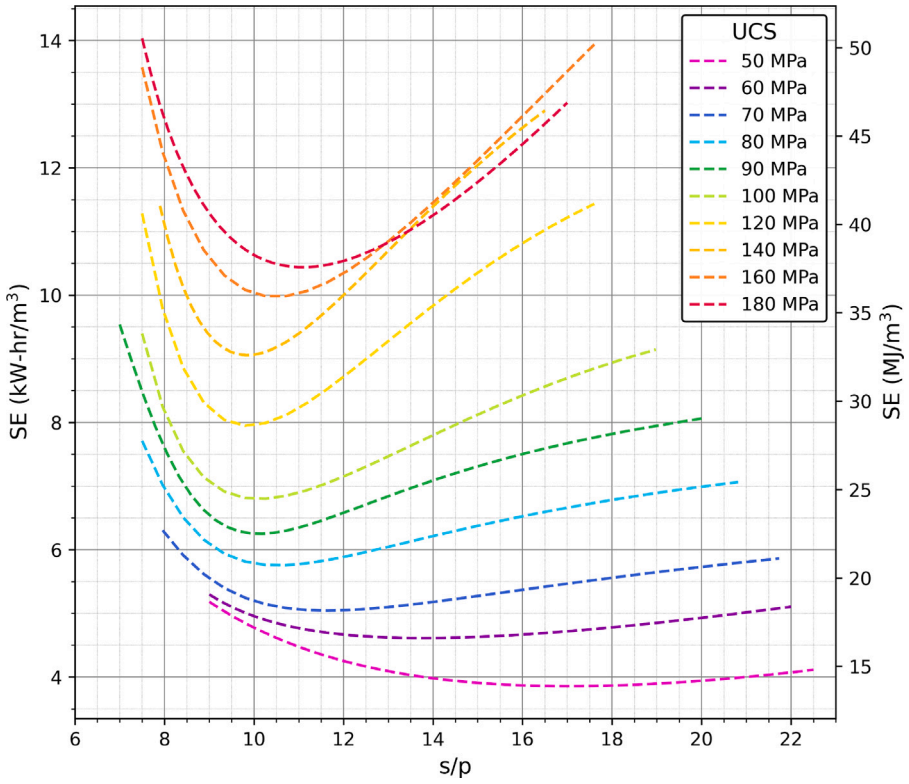

Fig. 13. $SE–s/p$ correlations across different UCS ranges, based on pressure distributions derived from amplified load profiles.

Table 1
Numerical model validation against experimental cutting data for different rock types.

Rock type	σ_c (MPa)	σ_t (MPa)	Cutter-disc (Type)	D (mm)	s/p Exp.	s/p Num.	SE_{exp} (MJ/m^3)	SE_{exp} (kW-h/m^3)	SE_{num} (kW-h/m^3)	Data resources
Limestone	63.6	8.86	CCS	432.0	18.00	13.15	5.83	1.62	4.64	Jeong et al.[38]
Limestone	65.6	7.40	CCS	432.0	10.00	11.09	14.76	4.10	4.81	Balci[39]
Kartal limestone	65.6	7.40	CCS	330.0	11.42	12.09	15.60	4.30	4.81	Copur et al.[40]
Nodular limestone	70.2	7.73	CCS	145.0	4.00	11.60	32.17	8.93	5.00	Comakli et al.[41]
Limestone - 2	77.9	4.90	S-RBC	305.0	10.00	11.03	18.76	5.20	5.45	Shaterpour et al.[42]
Carrara marble	79.0	14.0	V-TD	165.1	8.1	10.56	23.5	6.53	5.56	Cardu et al.[43]
Limestone - 1	81.78	5.17	S-RBC	305	8.3	10.41	40.29	11.19	5.83	Shaterpour et al.[42]
Skarn	88.4	5.94	S-RBC	305	20	10.3	31.72	8.81	8.19	Shaterpour et al.[42]
Granite - 2	91.3	10.1	CCS	432	12	10.27	11.52	3.2	3.08	Jeong et al.[38]
Gneiss - 2	91.5	15.2	CCS	432	12	10.27	14.69	4.08	6.3	Jeong et al.[38]
Lesotho basalt-NAB	97.2	12.9	CCS	432	9.41	10.41	26.39	7.33	6.73	Rostami[44]
Granodiorite	104.49	11.09	S-RBC	305	16.7	10.13	56.73	15.76	7.09	Shaterpour et al.[42]
Granite - 3	107.6	7.4	CCS	432	10	9.86	12.46	3.46	3.28	Jeong et al.[38]
Busan tuff	115.0	25.2	CCS	432	17	9.86	26.3	7.3	7.63	Cho et al.[17]
Tuff	115.5	25.2	CCS	432	15	9.86	6.44	1.79	7.63	Jeong et al.[38]
Diabase - 1	120.0	11.94	CCS	145	4	9.8	38.23	10.62	7.9	Comakli et al.[41]
Granite - 4	135.3	6.8	CCS	432	14	9.74	2.66	0.74	8.83	Jeong et al.[38]
Colorado spring granite	143.9	7.8	CCS	432	13.75	9.61	43.7	12.13	9.42	Rostami[44]
Granite - 6	145.5	7.8	CCS	432	15	9.74	2.48	0.69	9.33	Jeong et al.[38]
Felsite	145.5	9.5	CCS	432	14	9.74	9.46	2.63	9.33	Jeong et al.[38]
Diorite	158.5	11.2	CCS	432	10	10.71	13.0	3.61	9.99	Jeong et al.[38]
Beige marble	160	7.82	CCS	145	6.7	10.56	43.44	12.06	9.89	Comakli et al.[41]
Gneiss - 1	167.5	10.6	CCS	432	14	10.71	11.41	3.17	10.01	Jeong et al.[38]
Colorado red granite	178.5	8.9	CCS	432	17	11.19	37.44	10.4	10.21	Xu et al.[45]
Hwangdeung granite	183	9.8	CCS	432	11	11.03	52.8	14.67	10.35	Cho et al.[17]
Gneiss - 5	186	11.5	CCS	432	7.5	11.03	9.25	2.57	10.35	Jeong et al.[38]

where CCS is constant cross-section and V-TD is V type disc.

the validated UCS interval also exhibited outlier behaviour during validation, indicating local deviations associated with specific geological and operational conditions. This behaviour reflects the dependence of predictive reliability on the experimental coverage of the pressure distributions incorporated into the model. Since pressure-response characteristics vary with rock properties and cutting configuration, uncertainty increases under geological and operational conditions not represented within the available experimental database. Consequently, extending the methodology to broader engineering geological conditions requires additional experimentally derived pressure-distribution datasets.

To reduce the computational cost and algorithmic complexity of the previous numerical model, this study introduces a streamlined scheme

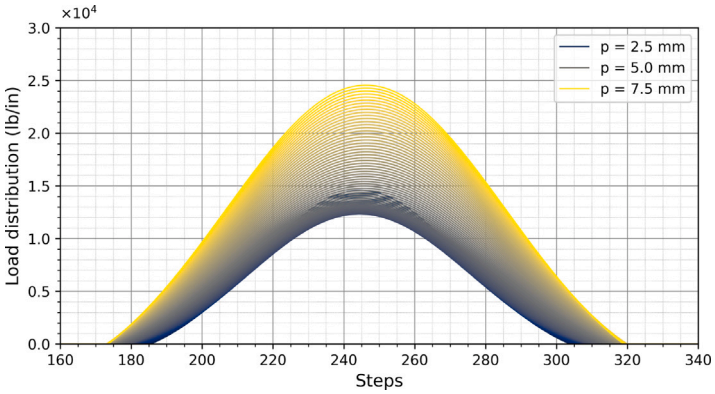

Fig. 14. Discrete data representation for Indiana Limestone at penetration depths of 2.5 mm, 5.0 mm, and 7.5 mm, derived from fitted Gaussian function parameters.

Table 2
Performance evaluation of predicted and experimental values for rocks with UCS below 115 MPa.

Parameter	SE	s/p
MAE (kW-h/m^3)	0.495	1.492
MAPE (%)	9.13	12.28
RMSE (kW-h/m^3)	0.565	2.01
R^2	0.909	0.62

where MAE is the Mean Absolute Error, MAPE is the Mean Absolute Percentage Error, RMSE is the Root Mean Square Error, and R^2 is the coefficient of determination.

Table 3
Polynomial coefficients for Gaussian distribution parameters for Colorado Red Granite.

$Parameter = a\,p^4 + b\,p^3 + c\,p^2 + d\,p + e$				
	P_0	P'	θ_c	ω
a	−182.1	172.9	-3.00×10^{-4}	4.00×10^{-4}
b	4134	−2983	-5.72×10^{-3}	-9.18×10^{-3}
c	-3.186×10^4	1.458×10^4	−0.0378	0.0624
d	9.063×10^4	−8924	0.120	−0.0793
e	-8.989×10^4	7.385×10^4	5.788	0.3973

P_0, P', θ_c, and ω are parameter outputs of Eq. (12) that fourth-degree polynomial, each dependent on p (penetration depth).

that still captures the rock–cutter interaction. In this context, the amplified load-pressure distributions (Fig. 11(b)) are decomposed into a series of Gaussian functions to characterize these distributions mathematically. After the initial parameter extraction, the functions are refined to better fit the actual contact range, followed by a re-estimation of the parameters. This iterative approach provides a Gaussian-based representation (Fig. 14) of the amplified load pressure distributions. The results (Table 3) reveal that each Gaussian parameter (Eq. (12)) strongly correlates with p, following a fourth-degree polynomial relationship. This result calls for a reassessment of the initial hypothesis, suggesting that although Gaussian functions offer a valid representation, their parameters systematically vary with penetration depth. This insight deepens the understanding of pressure profile behaviour and supports ongoing theoretical advancement and model refinement.

6. Conclusions

TBMs are widely adopted in rock tunnel construction due to their high advance rates and excavation safety. This study analyses the contact pressure distribution between the disc cutter and rock using LCM-derived parameters: p, s, and SE. The proposed methodology captures the nonlinear SE–s/p correlations and identifies optimal s/p ratios associated with minimum SE across different UCS intervals. These parameters are directly linked to TBM performance: p governs cutter normal force, thrust, torque, and penetration rate; s controls crack interaction and fragmentation efficiency; and SE quantifies cutting energy demand. Within the validated UCS range, the framework supports the assessment of TBM operational parameters, cutterhead design, and optimization of the rock-breaking process under minimum-SE conditions.

In the first model, after outlining the CSM model that originally characterizes disc-rock contact pressures, alternative contact pressure patterns were hypothesized, while maintaining the maximum contact pressure (Eq. (2)) value identified by the CSM model. However, these hypotheses on the contact pressure distribution did not allow for obtaining an acceptable SE pattern as the s/p ratio varies. These distributions, in fact, were unable to reproduce trends with minimum SE values and, therefore, with optimal s/p ratios. It is because the governing framework establishes that the cutting forces are primarily determined by the magnitude of the maximum contact pressure and the pressure distribution profile. The results show that the maximum contact pressure exerts a dominant influence on the resulting cutting forces. This dominant effect diminishes the contribution of the distribution profile, introducing a bias in force predictions. This imbalance contributes to the observed discrepancies between model outputs and theoretical expectations.

The pressure distribution represents the contact pressure generated beneath the disc cutter and governs the transfer of normal and rolling forces within the TBM rock-breaking mechanism. Indiana Limestone exhibits wide, symmetric distributions that remain stable with increasing penetration. From a mechanical perspective, this distribution indicates consistent force transfer, stable crushed-zone development, controlled crack propagation, and uniform chip formation. Colorado Red Granite follows a comparable trend with higher pressure concentration reflecting its greater UCS. Both behaviours are consistent with the error analysis, which showed that the proposed model produced more reliable SE predictions for rocks with UCS below 115 MPa, as reported in Table 2. In contrast, the localized pressure peaks characteristic of higher-UCS rocks indicate stronger force concentration and a more heterogeneous fragmentation process, increasing uncertainty in force and SE predictions.

The analyses clearly show that the optimal s/p ratio is relatively high, greater than 11 and up to 17, for rocks with low compressive strength (lower than 70 MPa). For medium-strength rocks, the optimal ratio tends to fall below 10, while for very high-strength rocks, it is approximately 10 or slightly higher. Furthermore, the minimum and optimal SE ranges from below 4 kWh/m^3 for low-strength rocks to over 10 kWh/m^3 for very high-strength rocks.

The decomposition of hybrid pressure distributions into Gaussian functions reveals a correlation between UCS and the associated Gaussian parameters. As UCS increases, the parameter ω decreases, indicating narrower distributions, while P' sharply increases, signifying

intensified peak pressures. Simultaneously, the parameter θ_c gradually shifts away from the symmetry axis. This evolving distribution shape introduces gradual uncertainty into the prediction model due to the high sensitivity of contact pressure as the cutter disc advances. Incorporating these trends into the comparative model analysis (Table 1) demonstrates that the model maintains robustness under low UCS; however, as rock strength increases, discrepancies between experimental and predicted outcomes become more pronounced.

Analysing laboratory test results and the available numerical models of disc-rock interaction gained detailed insights into rock failure and excavation mechanisms as a function of rock strength. The results emphasize the importance of accurately understanding the contact pressure distribution, which is fundamental for identifying the optimal s/p ratio corresponding to the minimum SE, representing the most efficient TBM disc excavation mode.

CRediT authorship contribution statement

Nestor Mejía: Writing – review & editing, Writing – original draft, Validation, Investigation, Formal analysis, Conceptualization. **Marilena Cardu:** Writing – review & editing, Supervision, Investigation, Formal analysis, Conceptualization. **Pierpaolo Oreste:** Writing – review & editing, Supervision, Formal analysis, Conceptualization.

Declaration of competing interest

The authors declare that they have no known competing financial interests or personal relationships that could have appeared to influence the work reported in this paper.

Appendix

Fig. 2 shows the pressure distribution patterns for different ψ values. When ψ is 0, the pressure distribution becomes uniform. As ψ approaches a value of 1, the pressure distribution transit to a linear distribution. Notably, the angle β adopts the half of angle ϕ when ψ is 0, highlighting the system's symmetry. In this sense, introducing the concept of centre of gravity in Eq. (15) enables an analytical solution for angle β in terms of ψ and ϕ with Eq. (16):

$$\beta = \frac{\int_0^{\phi} \theta \; P' \left(1 - \frac{\theta}{\phi}\right)^{\psi} d\theta}{\int_0^{\phi} \; P' \left(1 - \frac{\theta}{\phi}\right)^{\psi} d\theta} \tag{15}$$

$$\beta = \frac{\phi}{\psi + 2} \tag{16}$$

As expressed in Eq. (3), F_t is obtained through an analytical method. Consequently, Eq. (8) presents the general solution for the CSM model.

Two numerical approaches were conducted to validate the results of the general solution proposed in Eq. (8). The first approach uses the Taylor series expansion to approximate β as detailed in Eqs. (17).[18] An analytical solution then computes F_t (Eq. (3)), followed by the calculation of F_r (Eq. (6)). The second method calculates F_t and F_r by discretizing the parameter θ, as specified in Eq. (5). A third method, based on numerical integration, was developed using the trapezoidal rule with a resolution discretization of θ (0, ϕ, 1000).

$$\begin{bmatrix} F_{x'} \\ F_{y'} \end{bmatrix} = \sum_{i=1}^{n} (-1)^{(i-1)} \begin{bmatrix} \frac{\phi^{2i+\psi}}{(2i+\psi)(2i-2)!} \\ \frac{\phi^{2i-1+\psi}}{(2i-1+\psi)(2i-2)!} \end{bmatrix} \tag{17}$$

n is the number of iterations required to achieve the desired degree of accuracy in the numerical estimate, and γ denotes the angle of the resultant force in relative coordinates.

Table 4 lists the different SE values computed for the following input parameters: $R = 14\,\text{cm}$, $T = 2.5\,\text{cm}$, $s = 8\,\text{cm}$, $\sigma_c = 100\,\text{MPa}$, $\sigma_t = 11\,\text{MPa}$, and $\psi = 0.3$. Fig. 15 highlights the correlation between methods through the corresponding linear equation and the coefficient of determination (R^2). The slope of the linear equations approaches 1, supporting the validity of the analytical solution for the CSM.

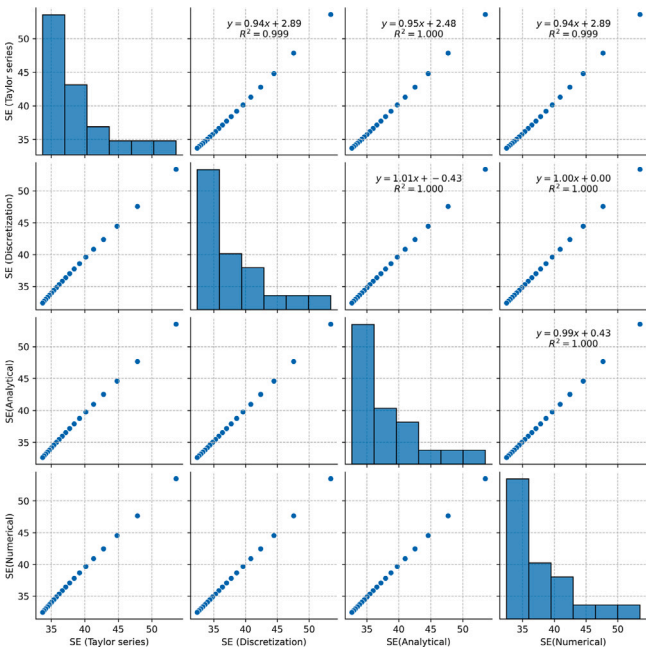

Fig. 15. Validation between results.

Table 4
Comparison of results used to validate the general solution of the CSM model.

ϕ (rad)	SE (Taylor series)	SE (Discretization)	SE (Analytical)	SE (Numerical)
0.084	53.605851	53.383971	53.518017	53.497181
0.119	47.848434	47.559434	47.692081	47.660224
0.146	44.806771	44.451417	44.587776	44.545557
0.169	42.789999	42.370147	42.511941	42.459819
0.189	41.305669	40.823082	40.971104	40.909422
0.207	40.144787	39.601024	39.755695	39.684722
0.224	39.199910	38.596340	38.757903	38.677859
0.239	38.408807	37.746641	37.915241	37.826311
0.254	37.732348	37.012669	37.188396	37.090736
0.268	37.144405	36.368189	36.551095	36.444845
0.281	36.626705	35.794840	35.984956	35.870235
0.293	36.165995	35.279292	35.476634	35.353551
0.305	35.752369	34.811579	35.016152	34.884803
0.317	35.378242	34.384060	34.595862	34.456335
0.328	35.037684	33.990757	34.209781	34.062156
0.339	34.725975	33.626909	33.853145	33.697494
0.350	34.439298	33.288663	33.522099	33.358491
0.360	34.174530	32.972864	33.213486	33.041981

Data availability

Data will be made available on request.

References

1. Meschke G. From advance exploration to real time steering of TBMs: A review on pertinent research in the Collaborative Research Center "Interaction Modeling in Mechanized Tunneling. *Tunn Undergr Sp. Technol.* 2018;3:1–20. http://dx.doi.org/10.1016/J.UNDSP.2018.01.002.
2. Farrokh E, Rostami J, Laughton C, Liu J. Analysis of unit supporting time and support installation time for open TBMs. *Rock Mech Rock Eng.* 2011;44:431–445. http://dx.doi.org/10.1007/s00603-011-0135-8.
3. Deng M. Challenges and thoughts on risk management and control for the group construction of a super-long tunnel by TBM. *Eng.* 2018;4:112–122. http://dx.doi.org/10.1016/J.ENG.2017.07.001.
4. Zou X, Zeng J, Yan G, Mohammed K, Abbas M, Abdullah N, Elattar S, Khadimallah M, Toghroli S, Escorcia-Gutierrez J. Advancing tunnel equipment maintenance through data-driven predictive strategies in underground infrastructure. *Comput Geotech.* 2024;173:106532. http://dx.doi.org/10.1016/J.COMPGEO.2024.106532.

5. Hassanpour J, Rostami J, Zhao J. A new hard rock TBM performance prediction model for project plannin. *Tunn Undergr Sp. Technol.* 2011;26:595–603. http://dx.doi.org/10.1016/J.TUST.2011.04.004.
6. Yang J, Yagiz S, Liu Y, Laouafa F. Comprehensive evaluation of machine learning algorithms applied to TBM performance prediction. *Undergr Sp.*. 2022;7:37–49. http://dx.doi.org/10.1016/J.UNDSP.2021.04.003.
7. Delisio A, Zhao J, Einstein H. Analysis and prediction of TBM performance in blocky rock conditions at the Lötschberg Base Tunnel. *Tunn Undergr Sp. Technol.* 2013;33:131–142. http://dx.doi.org/10.1016/J.TUST.2012.06.015.
8. Pan Y, Liu Q, Peng Q, Liu Q, Liu J, Huang X, Cui X, Cai T. Full-scale cutting tests to propose some empirical formulas for TBM disc cutter performance prediction. *Rock Mech Rock Eng.* 2019;52:4763. http://dx.doi.org/10.1007/s00603-019-01865-x.
9. Zare Naghadehi M, Samaei M, Ranjbarnia M, Nourani V. State-of-the-art predictive modeling of TBM performance in changing geological conditions through gene expression programming. *Meas.* 2018;126:46–57. http://dx.doi.org/10.1016/J.MEASUREMENT.2018.05.049.
10. Avunduk E, Copur H. Empirical modeling for predicting excavation performance of EPB tbm based on soil properties. *Tunn Undergr Sp. Technol.* 2018;71:340–353. http://dx.doi.org/10.1016/J.TUST.2017.09.016.
11. Liu Q, Liu J, Pan Y, Kong X, Hong K. A case study of TBM performance prediction using a Chinese rock mass classification system – Hydropower Classification (HC) method. *Tunn Undergr Sp. Technol.* 2017;65:140–154. http://dx.doi.org/10.1016/J.TUST.2017.03.002.
12. Feng S, Chen Z, Luo H, Wang S, Zhao Y, Liu L, Ling D, Jing L. Tunnel boring machines (TBM) performance prediction: A case study using big data and deep learning. *Tunn Undergr Sp. Technol.* 2021;110:103636. http://dx.doi.org/10.1016/J.TUST.2020.103636.
13. Yagiz S, Karahan H. Application of various optimization techniques and comparison of their performances for predicting TBM penetration rate in rock mass. *Int J Rock Mech Min Sci.* 2015;80:308–315. http://dx.doi.org/10.1016/J.IJRMMS.2015.09.019.
14. Li X, Zhang Y, Sun X. Numerical analysis for rock cutting force prediction in the tunnel boring process. *Int J Rock Mech Min Sci.* 2021;144:104696. http://dx.doi.org/10.1016/J.IJRMMS.2021.104696.
15. Hu X, Du C, Liu S, Tan H, Liu Z. Three-dimensional numerical simulation of rock breaking by the tipped hob cutter based on explicit finite element. *IEEE Access.* 2019;7:86054–86063. http://dx.doi.org/10.1109/ACCESS.2019.2925427.
16. Cho W, Jeon S, Jeonh H, Chang S. Evaluation of cutting efficiency during TBM disc cutter excavation within a Korean granitic rock using linear-cutting-machine testing and photogrammetric measurement. *Tunn Undergr Sp. Technol.* 2013;35:37–54. http://dx.doi.org/10.1016/j.tust.2012.08.006.
17. Cho W, Jeon S, Yu S, S. C. Optimum spacing of TBM disc cutters: A numerical simulation using the three-dimensional dynamic fracturing method. *Tunn Undergr Sp. Technol.* 2010;25:230–244. http://dx.doi.org/10.1016/j.tust.2009.11,007.
18. Rostami J, Ozdemir L. New model for performance production of hard rock TBMs. *Proc - Rapid Excav Tunneling Conf.* 1993:793–809.
19. Rostami J. Study of pressure distribution within the crushed zone in the contact area between rock and disc cutters. *Int J Rock Mech Min Sci.* 2013;57:172–186. http://dx.doi.org/10.1016/j.ijrmms.2012.07.031.
20. Zhang X, Ji P, Zhang Q, Liu Q, Wu S. Study of contact pressure distribution between cutter and rock surface using the discrete element method. *Int J Rock Mech Min Sci.* 2021;146:104875. http://dx.doi.org/10.1016/j.ijrmms.2021.104875.
21. Yang H, Wang H, Zhou X. Analysis on the rock–cutter interaction mechanism during the tbm tunneling process. *Rock Mech Rock Eng.* 2016;49:1073–1090. http://dx.doi.org/10.1007/s00603-015-0796-9.
22. Scolaro A, Fiorina C, Clifford I, Pautz A. Development of a semi-implicit contact methodology for finite volume stress solvers. *Internat J Numer Methods Engrg.* 2022;123:309–338. http://dx.doi.org/10.1002/NME.6857.
23. Van Wyk G, Els D, Akdogan G, Bradshaw S, Sacks N. Discrete element simulation of tribological interactions in rock cutting. *Int J Rock Mech Min Sci.* 2014;65:8–19. http://dx.doi.org/10.1016/J.IJRMMS.2013.10.003.
24. Ma H, Gong Q, Wang J, Yin L, Zhao X. Study on the influence of confining stress on TBM performance in granite rock by linear cutting test. *Tunn Undergr Sp. Technol.* 2016;57:145–150. http://dx.doi.org/10.1016/j.tust.2016.02.020.
25. Kang Y, Yang R, LYang L, Li C, Chen J, Zhu H, Liu N. Theoretical and numerical studies of rock breaking mechanism by double disc cutters. *Int J Min Sci Technol.* 2023;33:815–828. http://dx.doi.org/10.1016/j.ijmst.2023.03.006.
26. Xie W, Liu X, Zhang X, Yang X, Zhou X. A review of rock macro-indentation: Theories, experiments, simulations, and applications. *J Rock Mech Geotech Eng.* 2024;16:2351–2374. http://dx.doi.org/10.1016/j.jrmge.2023.07.022.
27. Pang S, Goldsmith W, Hood M. A force-indentation model for brittle rocks. *Rock Mech Rock Eng.* 1989;22:127–148.
28. Cook N, Hood M, Tsai F. Observations of crack growth in hard rock loaded by an indenter. *Int J Rock Mech Min Sci.* 1984;21:97–107. http://dx.doi.org/10.1016/0148-9062(84)91177-X.
29. Wang F, Ozdemir L. Tunnel-boring penetration rate and machine design. *Transp Res Rec.* 1978;3:21–28.
30. Zhang J, Li Y, Zhang Y, Yang F, Liang C, Tan S. Using a high-pressure water jet-assisted tunnel boring machine to break rock. *Adv Mech Eng.* 2020;12. http://dx.doi.org/10.1177/1687814020962290.
31. Yin L, Miao C, He G, Dai F, Gong Q. Study on the influence of joint spacing on rock fragmentation under TBM cutter by linear cutting test. *Tunn Undergr Sp. Technol.* 2016;57:137–144. http://dx.doi.org/10.1016/j.tust.2016.02.018.
32. Pan S, Goldsmith W. Investigation of crack formation during loading of brittle rock. *Adv Mech Eng.* 1990;23:53–63. http://dx.doi.org/10.1007/BF01020422.
33. Yin L, Miao C, He G, Dai F, Gong Q. Evaluation of rock muck using image analysis and its application in the TBM tunneling. *Tunn Undergr Sp. Technol.* 2021;113:103974. http://dx.doi.org/10.1016/j.tust.2021.103974.
34. Jeong H, Choi S, Lee S, Jeon S. Rock cutting simulation of point attack picks using the smooth particle hydrodynamics technique and the cumulative damage model. *Appl Sci.* 2020;10. http://dx.doi.org/10.3390/APP10155314.
35. Xue Y, Wang J, Zhou M, Liu J, Guo Y, Wamg J. Prediction of optimum TBM penetration strategy with minimum energy consumption in hard rocks. *Comput Geotech.* 2022;42:104844. http://dx.doi.org/10.1016/j.compgeo.2022.104844.
36. Gao J, He Y, Chen Y, Wang Z, Li C. Optimized binarization algorithm-based method for the image recognition and characterization of explosion damage in rock masses. *Eng Geol.* 2024;343:107787. http://dx.doi.org/10.1016/J.ENGGEO.2024.107787.
37. F. R, H. P. Rock excavation by disc cutter. *Int J Rock Mech Min Sci.* 1975;12:361–366. http://dx.doi.org/10.1016/0148-9062(75)90547-1.
38. Jeong H, Choi S, Lee Y. Evaluation of cutting performance of a TBM disc cutter and cerchar abrasivity index based on the brittleness and properties of rock. *Appl Sci.* 2023;13:2612. http://dx.doi.org/10.3390/APP13042612.
39. Balci C. Correlation of rock cutting tests with field performance of a TBM in a highly fractured rock formation: A case study in kozyatagi-kadikoy metro tunnel, Turkey. *Tunn Undergr Sp. Technol.* 2009;4:423–435. http://dx.doi.org/10.1016/j.tust.2008.12.001.
40. Copur H, Bilgin N, Tuncdemir H, Balci C. A set of indices based on indentation tests for assessment of rock cutting performance and rock properties. *J South Afr Inst Min Met.* 2003;103:589–599.
41. Comakli R, Balci C, Copur H, Tumac D. Experimental studies using a new portable linear rock cutting machine and verification for disc cutters. *Tunn Undergr Sp.*. 2021;108:103702. http://dx.doi.org/10.1016/J.TUST.2020.103702.
42. Mamaghani A, Copur H, Gumus A, Tumac D, Balci C, Erdogan T, Dogan E, Kocbay A. Full-scale linear cutting tests using a button cutter and deterministic performance prediction modeling for raise boring machines. *Tunn Undergr Sp. Technol.* 2022;127:104609. http://dx.doi.org/10.1016/j.tust.2022.104609.
43. Cardu M, Rispoli A, Iabichino G, Oreste P, Vagnon F. Theoretical and experimental results from laboratory tests by ILCM. *Geotech Geol Eng.* 2021;39:3573–3597. http://dx.doi.org/10.1007/s10706-021-01712-3.
44. Rostami J. *Design optimization, performance predictions, and economic analysis of TBM application in the proposed Yucca mountain nuclear waste repository* (Ms Thesis 4139). Colorado, USA, Colorado School of Mines.
45. Xu C, Zhu Y, Song D, Guo X, Liu X, Wang E, Lu R, Xu C, Zhu Y, Song D, Guo X, Liu X, Wang E, Lu R. Comparison of DEM models with different elemental dimensions for TBM disc cutter rock fragmentation. *Sustainability*. 2022;14:12909. http://dx.doi.org/10.3390/SU141912909.